

# Analytical And Experimental Output Performance Comparison Of Piezoelectric Energy Harvesters

UMOREN MFONOBONG ANTHONY

Department of Electrical/Electronic and Computer Engineering, University of Uyo, Uyo

Email: mfon4gigis@yahoo.com

**Abstract**— This paper presents the modelling and simulation of an oscillation-based piezoelectric energy harvester operated by aerodynamic ambient airflow for wireless sensors. It focuses on the comparative analysis of the performance validation of analytical model of piezoelectric energy harvester using ANSYS and the MATLAB model. The analytical modelled equations were validated by creating a complete virtual prototype of the piezoelectric energy harvester in Autodesk Inventor and exported to ANSYS for transient analysis. The summary of the comparison shows that the improvement over previous efforts has been proven to be very high. The airflow oscillation induced excitation force of 10.5 N was generated to excite the base structure and a power of 12900 mW was produced at third resonance frequency of 676.5 Hz.

**Keywords**— Piezoelectric , Crystal Lattice , Oscillation Induced Excitation Force , Remote Sensors , Electrical Energy , Energy Harvester

## I. INTRODUCTION

Piezoelectric energy harvesters are devices that convert ambient environmental vibration into electrical energy by absorbing ambient vibrations. The piezoelectric effect converts mechanical strain into electric current or voltage. It is based on the fundamental structure of a crystal lattice ((Rizman *et al.*, 2018; Hu *et al.*, 2018; Podder *et al.*, 2016).). Certain crystalline structures have a charge balance with negative and positive polarization, which neutralize along the imaginary polar axis. When this charge balance is perturbed with external stress onto the crystal mesh, the energy is transferred by electric charge carriers creating a current in the crystal (Akorode *et al.*, 2017; Nandi *et al.*, 2017). Conversely, with the piezoelectric effect an external charge input will create an unbalance in the neutral charge state causing mechanical stress (Zeng *et al.*, 2016; Ono *et al.*, 2016).

Some low-power electronic devices, for instance, remote sensors and portable electronic devices are powered by batteries. Long-lasting batteries have a restricted lifespan and have to be changed at intervals. The replacements process could be expensive when dealing with huge number of sensors in isolated or not easily accessible locations ((Sherazi *et al.*, 2018; Rashid *et al.*, 2018; Leon-Gil *et al.*, 2018).). For instance, where there is

not any conventional electricity supply in isolated localities, submerged and other difficult-to-access environments, these devices and sensors are being driven by batteries or wires. The electricity supply limits the wide deployment and development for these wireless sensors. For example, the difficulties in using electronic devices to monitor crude oil pipeline passing through a forest. Energy harvesting is the most promising way of overcoming the challenges currently presented by finite life power sources like batteries (Elfrink *et al.*, 2016; Mackenzie and Ho, 2015; Iranmanesh *et al.*, 2018; Halim *et al.*, 2017). The process of energy harvesting involves the harnessing of ambient energy from within the vicinity of the sensor device and converting this energy into usable electrical energy. Piezoelectric energy harvesting is one of the most efficient systems of energy harvesting, hence it is currently a very active area of research (Khan and Iqbal, 2018).

## II. WORKFLOW FOR MODELLING OF PIEZOELECTRIC ENERGY HARVESTER

An aeroelastic piezoelectric energy harvester which uses vibration induced by ambient air flow for electricity generation is proposed. The system is made up of an airfoil wing, three linear springs and a torsional spring, serving as a base structure for the attachment of the piezoelectric cantilever beam.

The airfoil is modelled from first principles with the application of Newton's second law and Lagrange's equations to obtain an uncoupled aero elastically induced flutter and vortex heaving and pitching vibratory equations of motion for the airfoil wing. The beam will be modelled by applying Euler-Bernoulli beam theory to develop an uncoupled differential equation of motion of the beam. Aero-structural and electromechanically coupling were performed to obtain models for the voltage, current and power responses of the system.

The analytical models of the energy harvester will be validated by using finite element analysis (FEA) solver of the ANSYS simulation software. Three-dimensional (3D) model of the system will be developed in Autodesk Inventor which will comprise of a frame, a set of metal blocks for linear and torsional springs, airfoil shaped wing and cantilever beam. This 3D model developed in Autodesk Inventor will be export to ANSYS for electrical transient analysis, to determine the amount of power, voltage and current from the energy harvester. The diagram in Figure 1 shows the workflow to modelling and analyzing the aeroelastically induced vibration for energy harvesting of the piezoelectric energy harvester.

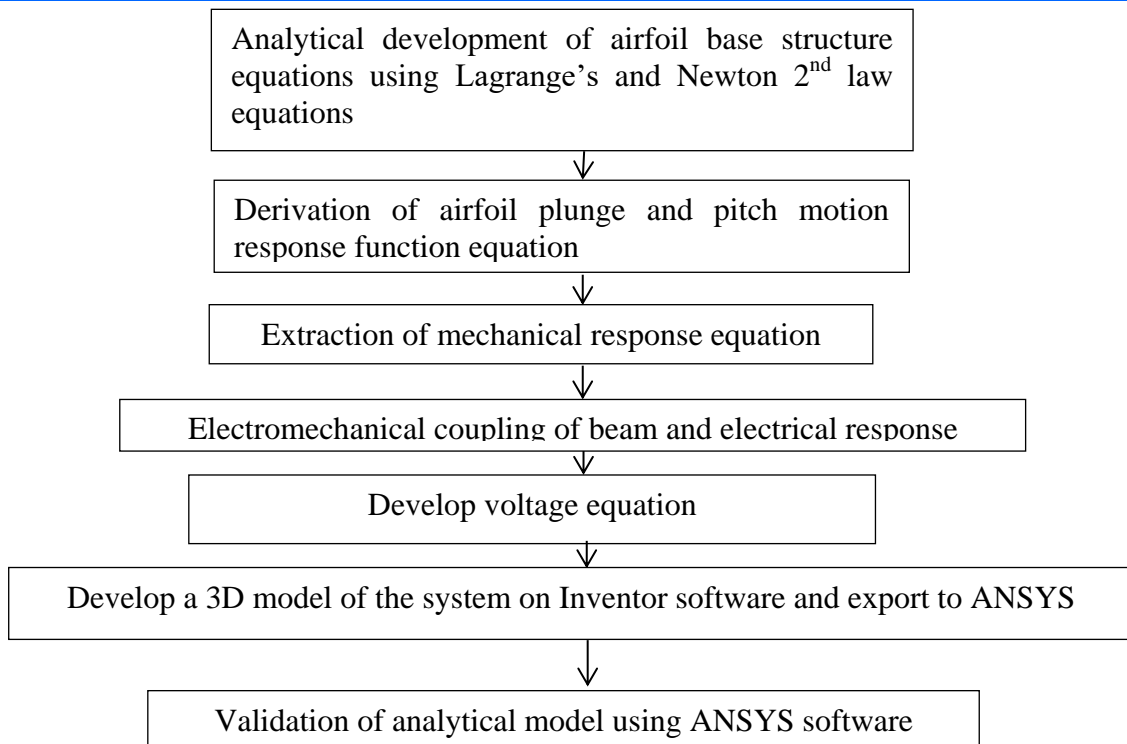


**Figure 1: Workflow for modelling the piezoelectric energy harvester.**

### III. AEROELASTIC PIEZOELECTRIC ENERGY HARVESTER SYSTEM

The proposed aeroelastic energy harvester is shown in Figure 2, and comprises of a 2-DoF airfoil wing, modelled as a dynamically oscillating base structure for the attachment of the piezoelectric cantilever beam. The two degrees of freedom for the airfoil is the heaving motion ( $h$ ) and the pitching ( $\alpha$ ) of the airfoil as ambient air flows over it. The cantilever beam is a bimorph

piezoelectric beam, which has its upper and lower surfaces covered with piezoceramic layers with an Aluminium substructure. In this research, the airfoil motion is designed to attain flutter and the beam is structurally modelled with the aid of Euler-Bernoulli theory. As clearly shown in the diagram, the aeroelastic system is constrained to move or oscillate in two degrees of freedom with a series of three translational springs in the plunge direction and a torsional spring in the pitching direction.

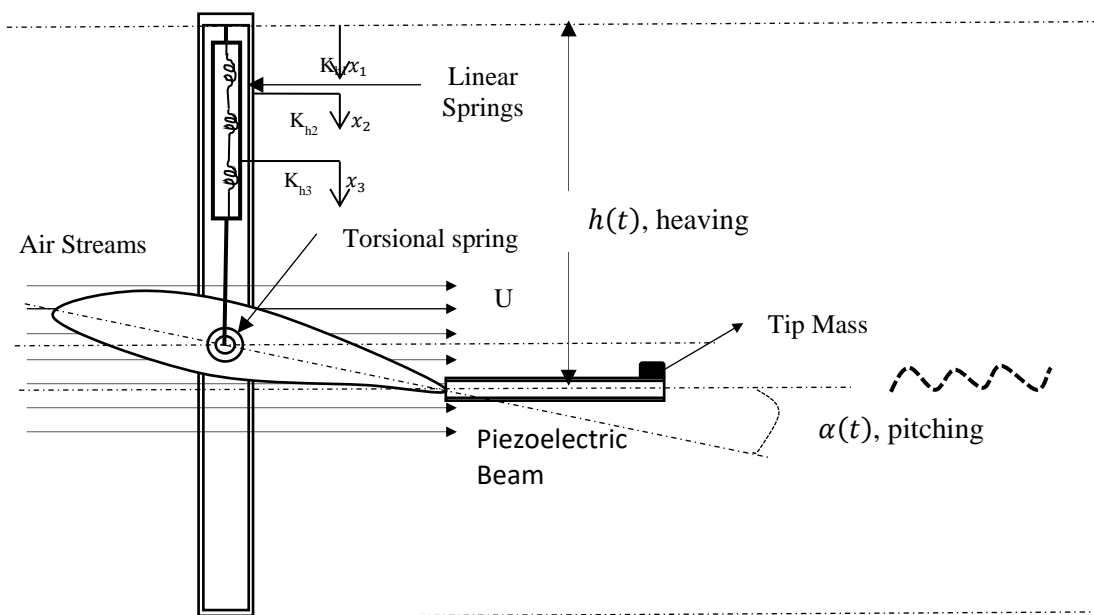


**Figure 2: Cross sectional view of piezoelectric energy harvester setup.**

Source: Formulated by the researcher (2019).

The essence of the three linear springs in series is to further enhance the plunge displacements which in turn increase the rate of vibration and mechanical strain of the piezoelectric beam. The linear and torsion springs are attached to the elastic axis of the airfoil. The linear springs have spring constants of  $k_{h1}$ ,  $k_{h2}$ , and  $k_{h3}$ , and their corresponding displacements or strains are  $x_1$ ,  $x_2$ , and  $x_3$  respectively. There are nonlinear dampers incorporated in the plunge and pitch directions with damping coefficients denoted as  $d_h$  and  $d_\alpha$ . The structural damping is placed within the system to help maintain stability and as a means of controlling the speed at which flutter occurs. Other variables in the figure include mass of airfoil per unit span

of wing  $m_a$ , mass of cantilever beam  $m$ , tip mass  $m_t$ , length of cantilever beam  $L$ , and freestream airflow velocity  $V$ .

#### IV. MODELLING OF AIRFOIL BASE STRUCTURE DYNAMICS

The piezoelectric cantilever beam and the airfoil offered a compound component  $F_t(x, t)$ , comprising of force and moment generated by the aeroelastic system as the wind flows over the structure (airfoil), serving as a main source of oscillation of the attached piezoelectric cantilever beam.

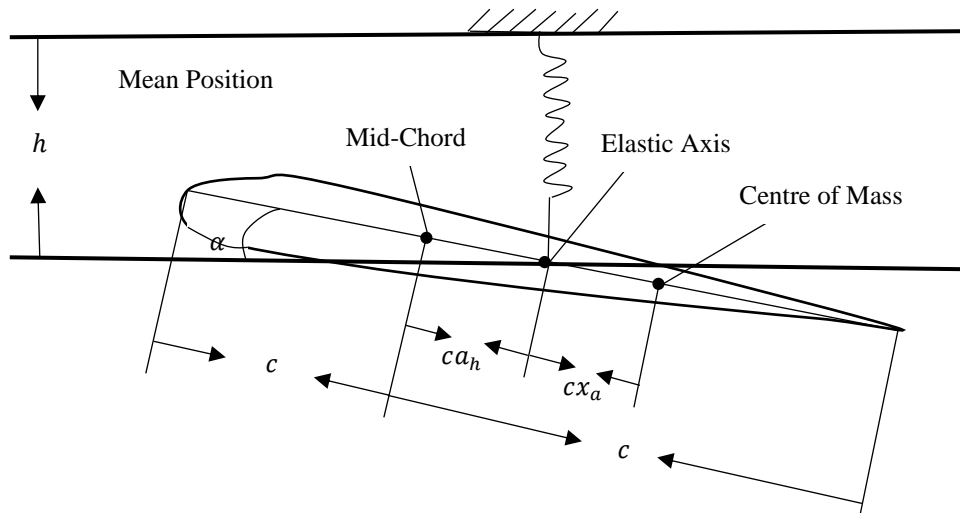


**Figure 3: Schematic of a two-degree-of-freedom airfoil structural section.**  
 Source: Alighanbari (1995).

The diagram in Figure 3, shows a simplified aeroelastic system. It consists of a rigid two-dimensional airfoil mounted on torsional and translational springs. The point of attachment of the spring (elastic axis) is located at the shear center of the airfoil at which a shear force can be applied without producing a rotation. In Figure 3.3, the plunging deflection is denoted by  $h$  measured at the elastic axis and positive in the downward direction, and  $\alpha$  is the pitch angle about the elastic axis. The elastic is located at a distance  $ca_h$  from the mid-chord, mass center is located at a distance  $cx_a$  from the elastic axis,  $c$  is the semi-chord length, the pitch angle of the airfoil is denoted by  $\alpha$ ,  $x_a$  is the nondimensional (dimensionless) distance from elastic axis to center of mass and  $a_h$  is the nondimensional (dimensionless) distance from elastic axis to mid-chord.

There are mainly two aspects to aeroelastic system modelling: the structural model and aerodynamic model.

#### Uncoupled Equations of the 2-D Aeroelastic Airfoil Wing System

For this research, Lagrange equation and Newton's second law (Force = mass  $\times$  acceleration) of motion was adopted. The equation of motion adopted from previous model by Guruswamy and Yang (1981) and modified to incorporate the attached section of the cantilever beam and the three linear plunge springs.

Considering the free body diagram in Figure 3, the lift force generated by the airfoil is controlled by the plunge linear spring and damper mechanism at the elastic axis of the airfoil. The combined linear springs in series yields an equivalent spring constant of  $k_{eq}$  is:

$$k_{eq} = \frac{k_{h1}k_{h2}k_{h3}}{k_{h1}+k_{h2}+k_{h3}} \quad (1)$$

where  $k_{h1}$ ,  $k_{h2}$ , and  $k_{h3}$  are the individual spring constants for the three linear springs in plunge degree of freedom. The lift force will cause a corresponding total plunge displacement of:

$$h = x_1 + x_2 + x_3 \quad (2)$$

where  $x_1$ ,  $x_2$ , and  $x_3$  are the individual spring displacement for the three linear springs.

The equation for the lift and pitching moment (Lagrange equation) of the airfoil was obtained from an article by Guruswamy and Yang (1981) as represented in Equation 3 and Equation 5. There is a single robust structural spring damper that cushions the spring movement, and under equilibrium conditions, the force balance on the system is:

$$m_a \frac{d^2h}{dt^2} + m_a cx_a \frac{d^2\alpha}{dt^2} + k_h h + d_h \frac{dh}{dt} = -L(h, \alpha, t) \quad (3)$$

where  $m_a$  is the mass of airfoil per unit span of wing,  $k_h$  is the spring constant,  $d_h$  is the damping coefficient of the plunge,  $h$  is the plunge displacement,  $c$  is the semi-chord length,  $x_a$  is the nondimensional distance from elastic axis

to centre of mass and  $L(h, \alpha, t)$  is the aerodynamic lift force.

Substituting Equation 2 and Equation 1 into Equation 3, the lift force for the displacement of three springs and equivalent linear spring constant ( $k_{eq}$ ) in series is given as:

$$m_a \frac{d^2 h}{dt^2} + m_a c x_a \frac{d^2 \alpha}{dt^2} + k_{eq} (x_1 + x_2 + x_3) + d_h \frac{dh}{dt} = -L(h, \alpha, t) \quad (4)$$

where  $h = (x_1 + x_2 + x_3)$ ,  $k_h = k_{eq} = \frac{k_{h1} k_{h2} k_{h3}}{k_{h1} + k_{h2} + k_{h3}}$ ,  $c$  is the semi-chord length and  $x_a$  is the nondimensional distance of the centre of mass from the elastic axis.

Taking the moments about the elastic axis yields the governing equation for the pitching moment of the system as:

$$m_a x_a c \frac{d^2 h}{dt^2} + J_\alpha \frac{d^2 \alpha}{dt^2} + k_\alpha \alpha + d_\alpha \frac{d\alpha}{dt} + k_h h c \alpha_n = M(h, \alpha, t) \quad (5)$$

where  $J_\alpha$  is the airfoil moment of inertia about the centre of mass,  $h$  is the plunge displacement,  $d_\alpha$  is the torsion

spring damping coefficient,  $a_h$  is the nondimensional distance of the elastic axis from the mid-chord,  $k_\alpha$  is the torsion spring constant,  $k_h$  is the linear spring constant,  $x_a$  is the non-dimensional distance of the centre of mass from the elastic axis,  $c$  is the semi-chord length and  $M$  is the pitching moment.

Substituting Equation 3.2 in Equation 3.5, the pitching moment for the system becomes:

$$m_a x_a c \frac{d^2 h}{dt^2} + J_\alpha \frac{d^2 \alpha}{dt^2} + k_\alpha \alpha + d_\alpha \frac{d\alpha}{dt} + k_{eq} (x_1 + x_2 + x_3) c \alpha_n = M(h, \alpha, t) \quad (6)$$

where  $k_h = k_{eq} = \frac{k_{h1} k_{h2} k_{h3}}{k_{h1} + k_{h2} + k_{h3}}$

Considering an uncouple airfoil structurally attached with a section of a piezoceramic beam at the trailing edge as shown in Figure 4, where A is airfoil mid-span, E is the elastic axis, CG is the centroid of the airfoil,  $L$  is the actual airfoil lift,  $h_p$  is the piezoceramic layer thickness,  $h_s$  is the thickness of substructure,  $b$  is width of the beam, and  $c$  is the airfoil semi-chord.

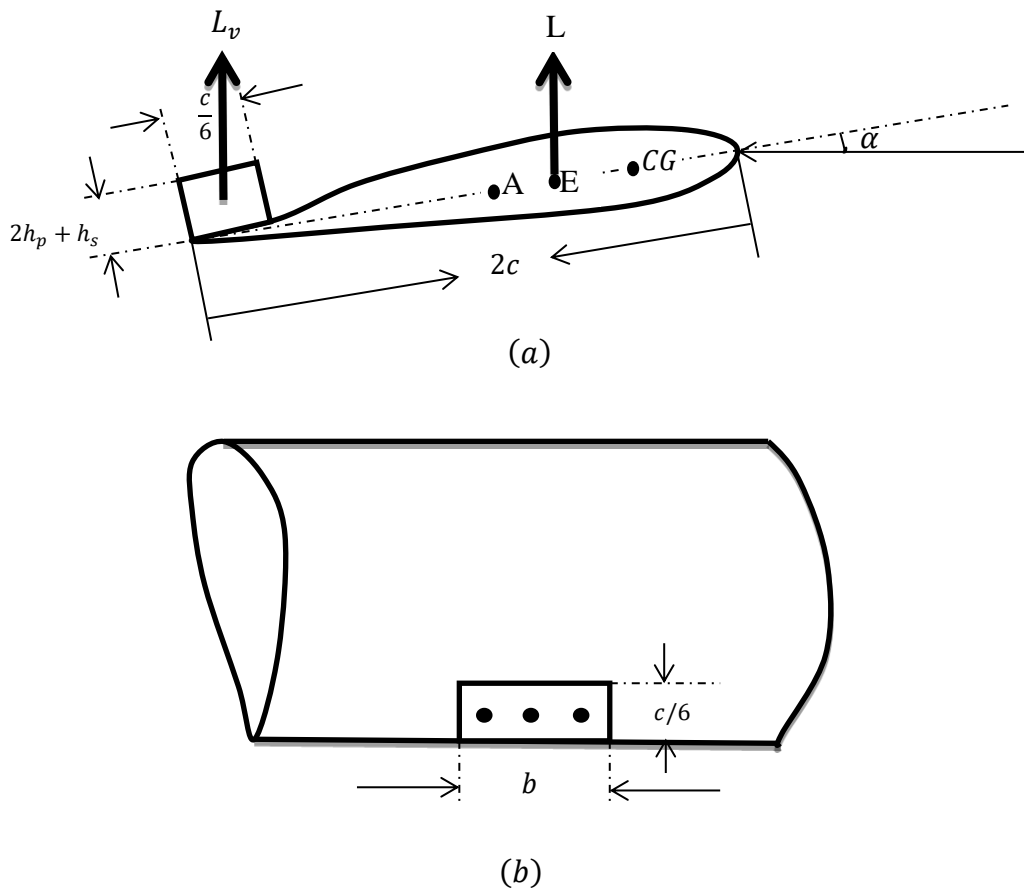


Figure 4: Uncoupled airfoil attached to a sectional beam.

Half the attached section of the piezoceramic beam is  $\frac{c}{6} \div 2 = \frac{c}{12} = 0.083c$  ( $1c - 0.083c = 0.917c$ ). This uncoupled part of the beam introduces vortex shedding at the trailing edge of the airfoil, which will result in an added vortex induced vibrations to the system.

Assuming the attached section of the piezoceramic beam of length of  $c/6$ , at the trailing edge is factored into the analysis as shown in Figures 4, the aerodynamic forces and moments will be greatly affected.

According to the Anderson (2001), the uncoupled beam section can exhibit a secondary lift force or vortex lift given by:

$$L_v = \frac{\rho \gamma^2}{2\pi r} \int_0^l dY dY \quad (7)$$

where  $\rho$  is the air density,  $\gamma$  is vortex strength per unit length,  $r$  is the radius of the vortex curve ( $r = h/\sin\theta$ ) and  $l$  is the length of the vortex flow within the end of the airfoil wing and  $Y$  is the unit length of the vortex sheet considered at a particular point.

Considering the short span of the uncoupled beam, only one vortex sheet curve is considered to be initiated at a point along plunge distance ( $h$ ) away from the surface of beam. The vortex curve is at a distance of  $r$ , from a point and making an angle of  $\theta$  with the beam. Therefore vortex radius can be expressed in terms of the plunge as  $r = h/\sin\theta$  and the vortex flow length at the end of the airfoil wing can be expressed as  $l = \frac{c}{6}$  (where:  $\frac{c}{6}$  is the assumed length of the sectional beam attached to the airfoil). Integrating the double integral in Equation 3.7 and substituting the value of  $r$  and  $l$ , the equation for the vortex lift becomes:

$$L_v = -\frac{\rho c^2 \gamma^2}{72\pi h} \sin\theta \quad (8)$$

Also, the uncoupled beam mass exerts a force that opposes the vortex induced lift, and it is given as:

$$F_n = m \frac{d^2 h}{dt^2} \quad (9)$$

where  $m$  is the mass per unit length of the beam.

Based on Figure 5, the uncoupled beam section experience a lift force which acts normally to its surface, and this is different from the lift generated by the airfoil whose point of action coincide with elastic axis or centre of pressure (CP). This vortex lift force is highest when the pitch angle increases to its highest value, causing the CP of the airfoil to move from its original position towards aerodynamic centre (AC) (that is when airfoil becomes almost vertical). At  $\alpha \gg 0$ , the distance between  $F_n$  and the elastic axis or CP where the springs are attached would be  $(0.9c + cx_\alpha)$  because the CP moves towards aerodynamic centre, causing the elastic axis or CP to be situated between the AC and mid-span. However, at  $\alpha = 0$  the distance becomes  $(0.9c - ca_h)$ , indicating that the CP has moved beyond the middle of airfoil.

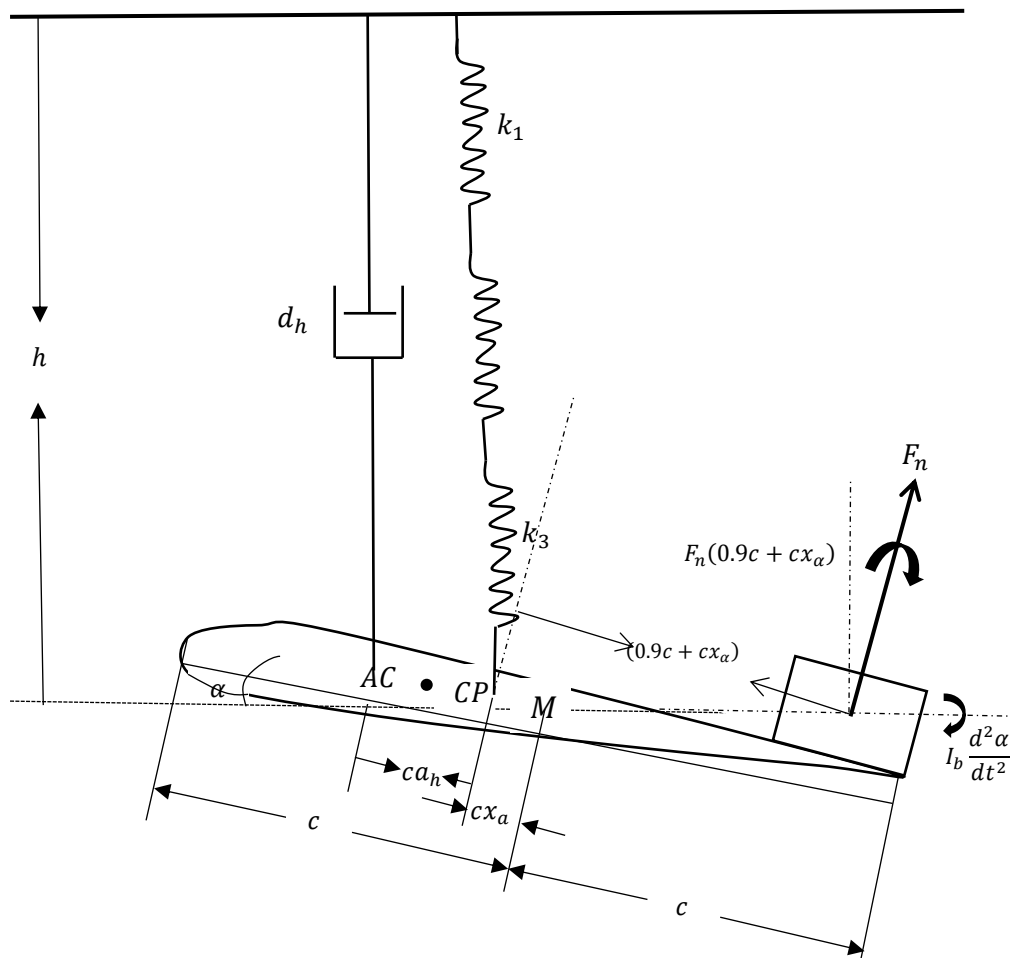


**Figure 5: Uncoupled beam section showing vortex and airfoil forces and moments.**

As the vortex sheds around the uncoupled section and beyond, the vortex sheets around the mass assumed the heaving motion acceleration and the circular

acceleration of the airfoil pitching motion. Hence, the uncoupled beam section experiences a moment and inertia about the elastic axis and this can be expressed as the total moment induced by the beam:

$$M_n = m \frac{d^2 h}{dt^2} (0.9c + cx_\alpha) + I_b \frac{d^2 \alpha}{dt^2} \quad (10)$$

where  $I_b$  is the moment of inertia of the uncoupled beam. Substituting Equation 8 and Equation 9 in Equation 4 as the secondary lift and substituting Equation 10 in Equation 6 as the secondary moment components:

$$(m_a + m) \frac{d^2 h}{dt^2} + m_a x_\alpha c \frac{d^2 \alpha}{dt^2} + d_h \frac{dh}{dt} + k_{eq} h + \frac{\rho c^2 \gamma^2}{72\pi h} \sin \theta = -L(h, \alpha, t) \quad (11)$$

$$[m(cx_\alpha + 0.9c) + m_a x_\alpha c] \frac{d^2 h}{dt^2} + (J_\alpha + I_b) \frac{d^2 \alpha}{dt^2} + d_\alpha \frac{d\alpha}{dt} + k_\alpha \alpha + k_{eq} h c \alpha_h = M(h, \alpha, t) \quad (12)$$

In Autodesk inventor software, the bounded length of the attached beam is taken as  $c/6$ , then the height is  $2h_p + h_s = c/6$ , and the width is  $b = c/3$ , where  $h_p$  is the thickness of the piezoceramic layers, and  $h_s$  is the

thickness of the beam's substructure. Let the mass density ( $density = \frac{mass}{volume}$ ) of the composite beam be  $\rho_c$ , then the mass of the uncoupled beam can be expressed as:

$$m = \rho_c \frac{c^3}{108} \quad (13)$$

There is another moment component which is due to the inertia of the uncoupled mass, acting about the line of symmetry of the beam. Assuming the pitch angle increases, the CP moves forward and the pitch angle will increase also. This means that the mass of the beam times the square of the perpendicular distance  $d$ , between the elastic axis of the airfoil and the centre of gravity of the uncoupled beam mass. From the diagram in Figure 6,  $d = (0.9c - c\alpha_h) \cos \alpha_0$ , where  $\alpha_0$  is the pitch angle made by the uncoupled beam. The value of  $\alpha_0$  is assumed to be the same as the airfoil pitching angle  $\alpha$ . Therefore the uncoupled beam moment of inertia can be expressed as:

$$I_b = m d^2 = \rho_c \frac{c^3}{108} (0.9c - c\alpha_h)^2 \cos^2 \alpha_0 \quad (14)$$

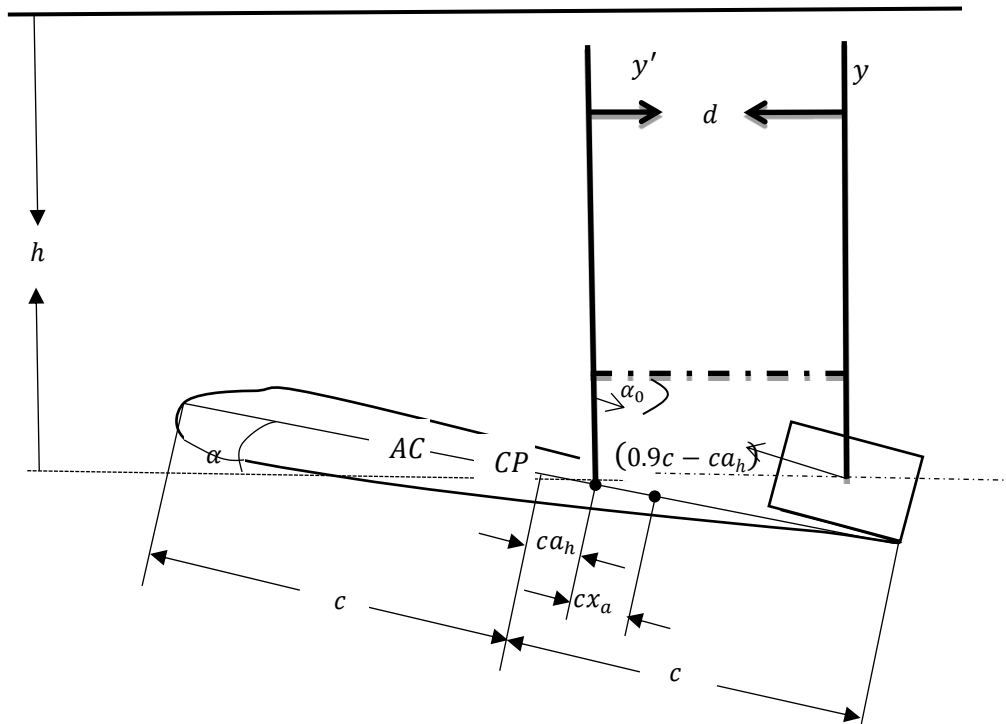


**Figure 6: Determination of mass moment of inertia of uncoupled beam.**

In order to express Equations 11 and Equation 12 in purely airfoil parameters, the uncoupled part of the beam's dimensions must be scaled down to the airfoil dimensions by the introduction of dimensionless air-speed ( $U$ ). This will allow a proper expression for the beam mass and moment of inertia to be derived in terms of the airfoil geometric and physical properties (Yining *et al.*, 2016; Dias *et al.* 2013). Substituting the mass of the uncoupled beam (Equation 13) into Equation 11. Substituting Equation 13 and 14 into Equation 12 and multiplying the differential component of Equation 11 and Equation 12 by  $\frac{U}{c}$  and  $\frac{U^2}{c^2}$  the airfoil motion equations are given finally as:

$$\left( m_a + \rho_c \frac{c^3}{108} \right) \frac{U^2}{c^2} \frac{d^2 h}{dt^2} - m_a x_\alpha c \frac{U^2}{c^2} \frac{d^2 \alpha}{dt^2} + d_h \frac{U}{c} \frac{dh}{dt} + k_{eq} h + \frac{\rho c^2 \gamma^2}{72\pi h} \sin \theta = -L(h, \alpha, t) \quad (15)$$

$$\left[ \rho_c \frac{c^3}{108} (cx_\alpha + 0.9c) + m_a x_\alpha c \right] \frac{U^2}{c^2} \frac{d^2 h}{dt^2} + \left( J_\alpha + \rho_c \frac{c^3}{108} (0.9c - c\alpha_h)^2 \cos^2 \alpha_0 \right) \frac{U^2}{c^2} \frac{d^2 \alpha}{dt^2} + d_\alpha \frac{U}{c} \frac{d\alpha}{dt} + k_\alpha \alpha + k_{eq} h c \alpha_h = M(h, \alpha, t) \quad (16)$$

Equation 15 and 16 is converted to dimensionless equations to reduce the complexity of the problem, where some parameters might be small enough to be ignored or treated approximately, so that the stability analysis of the uncoupled system can be carried out. According to Alighanbari (1995) the natural frequencies of the

uncoupled system in terms of the airfoil mass and moment of inertia about the elastic axis are given as:

$$\omega_h = \sqrt{\frac{k_{eq}}{m_a}} \quad (17)$$

and

$$\omega_\alpha = \sqrt{\frac{k_\alpha}{J_\alpha}} \quad (18)$$

Substituting Equation 17 and Equation 3.18 into Equation 15 and Equation 16 respectively, the lift and moment equation becomes:

$$\left(m_a + \rho_c \frac{c^3}{108}\right) \frac{U^2}{c^2} \xi''(\tau) - m_a x_\alpha c \frac{U^2}{c^2} \alpha''(\tau) + d_h \frac{U}{c} \xi'(\tau) + m_a \omega_h^2 \xi(\tau) + \frac{\rho c^2 \gamma^2}{72\pi \xi(\tau)} \sin \theta = -L(h, \alpha, \tau) \quad (19)$$

$$\left[\rho_c \frac{c^3}{108} (cx_a + 0.9c) + m_a x_\alpha c\right] \frac{U^2}{c^2} \xi''(\tau) + \left(J_\alpha + \rho_c \frac{c^3}{108} (0.9c - cx_\alpha)^2 \cos^2 \alpha_0\right) \frac{U^2}{c^2} \alpha''(\tau) + d_\alpha \frac{U}{c} \alpha'(\tau) + J_\alpha \omega_\alpha^2 \alpha(\tau) + m_a \omega_h^2 \xi(\tau) c^2 \alpha_h = M(h, \alpha, \tau) \quad (20)$$

where  $\frac{d^2 h}{dt^2} = \xi''(\tau)$ ,  $\frac{dh}{dt} = \xi'(\tau)$ ,  $\frac{d^2 \alpha}{dt^2} = \alpha''(\tau)$ ,  $\frac{d\alpha}{dt} = \alpha'(\tau)$  and prime denotes differentiation with respect to non-dimensional time  $\tau$ .

Dividing Equation 19 by  $m_a \frac{U^2}{c^2}$ , and substituting  $c = \frac{1}{\omega_h}$ , then the plunge equation is reduce to:

$$\left(1 + \rho_c \frac{1}{\omega_h^4 108 m_a}\right) \xi''(\tau) - \frac{1}{\omega_h} x_\alpha \alpha''(\tau) + d_h \frac{1}{\omega_h m_a U} \xi'(\tau) + \frac{1}{\omega_h^2} \xi(\tau) + \frac{\rho \gamma^2}{72\pi m_a \omega_h^3 U^2 \xi(\tau)} \sin \theta = p(\tau) \quad (21)$$

where  $\xi(\tau)$  is the non-dimensional plunge displacement of the elastic axis,  $\xi = h/c$

Dividing Equation 20 by  $J_\alpha \frac{U^2}{c^2}$ , and substituting  $c = \frac{1}{\omega_\alpha}$ , then the pitch equation is reduce to:

$$\left[\rho_c \frac{1}{\omega_\alpha^4 108} (x_a + 0.9) \frac{1}{J_\alpha} + \frac{x_\alpha}{\tau_\alpha^2}\right] \xi''(\tau) + \left(1 + \rho_c \frac{1}{\omega_\alpha^5 108 J_\alpha} (\alpha_h^2 - 1.8\alpha_h + 0.81) \cos^2 \alpha_0\right) \alpha''(\tau) + d_\alpha \frac{1}{\omega_\alpha J_\alpha U} \alpha'(\tau) + \frac{1}{U^2} \alpha(\tau) + m_a \omega_h^2 \frac{1}{\omega_\alpha^2 J_\alpha U^2} \xi(\tau) \frac{1}{\omega_\alpha^2} \alpha_h = r(\tau) \quad (22)$$

Finally, the equations of motion can be written in non-dimensional form. Hence the final airfoil wing base structure equations of motions are represented as:

$$\ell_{h1} \xi''(\tau) - \ell_{h3} x_\alpha \alpha''(\tau) + \zeta_\xi \frac{1}{U} \xi'(\tau) + \ell_{h4} \xi(\tau) + \frac{\ell_{h2}}{\xi(\tau)} = p(\tau) \quad (23)$$

$$\left[\kappa_{h1} + \frac{x_\alpha}{\tau_\alpha^2}\right] \xi''(\tau) + \kappa_\alpha \alpha''(\tau) + \zeta_\alpha \frac{1}{U} \alpha'(\tau) + \frac{1}{U^2} \alpha(\tau) + \kappa_{h2} \left(\frac{\bar{\omega}}{U}\right)^2 \xi(\tau) = r(\tau) \quad (24)$$

where

$$\ell_{h1} = \left(1 + \rho_c \frac{1}{\omega_h^3 108 m_a}\right), \ell_{h2} = \frac{\rho \gamma^2}{72\pi m_a \omega_h^3 U^2} \sin \theta, \ell_{h3} = \frac{1}{\omega_h}, \ell_{h4} = \frac{1}{U^2 \omega_h}, \kappa_{h1} = \rho_c \frac{1}{\omega_\alpha^4 108} (x_a + 0.9) \frac{1}{J_\alpha}, \kappa_\alpha = \left(1 + \rho_c \frac{1}{\omega_\alpha^5 108 J_\alpha} (\alpha_h^2 - 1.8\alpha_h + 0.81) \cos^2 \alpha_0\right), \kappa_{h2} = \frac{m_a \alpha_h}{J_\alpha \omega_\alpha^2}, \zeta_\xi = d_h / m_a \omega_h \text{ and } \zeta_\alpha = d_\alpha / J_\alpha \omega_\alpha \text{ represent the damping ratios in plunge and pitch, the non-dimensional radius of gyration about the elastic is } \tau_\alpha = \sqrt{J_\alpha / m_a c^2}, \text{ the non-dimensional force is } p(\tau) = -L(h, \alpha) c^2 / m_a U^2, \text{ the non-dimensional moment is } r(\tau) = M(h, \alpha) c^2 / J_\alpha U^2, \text{ and the frequency ratio is defined as } \bar{\omega} = \omega_h / \omega_\alpha.$$

## V. VALIDATION OF ANALYTICAL MODEL OF PIEZOELECTRIC ENERGY HARVESTER USING ANSYS

The analytical modelled Equations are validated by creating a complete virtual prototype of the piezoelectric energy harvester in Autodesk inventor and exported to ANSYS for transient analysis.

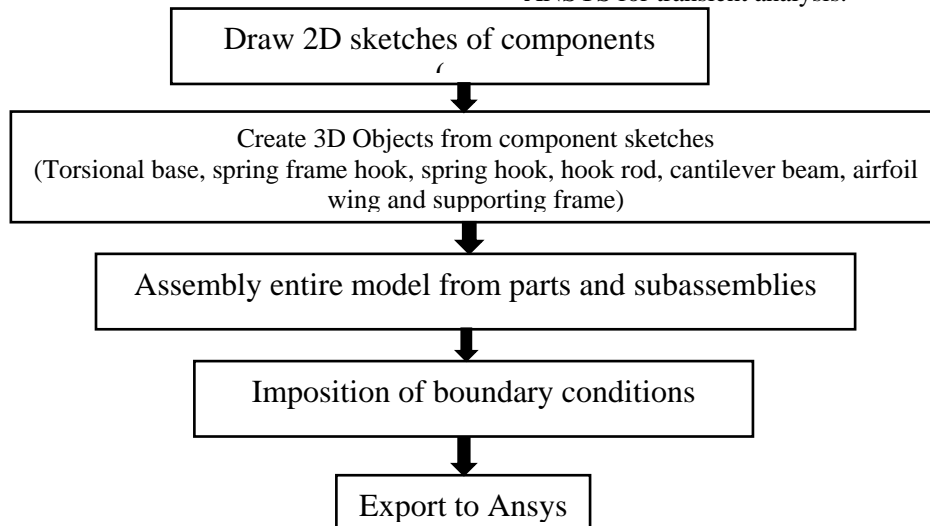
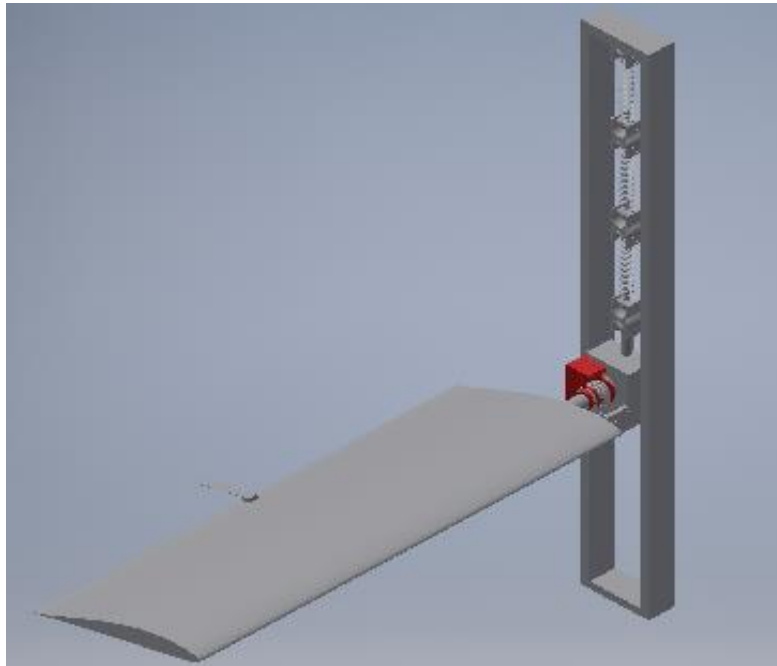


Figure 7: Flowchart of creating 3D model of the piezoelectric energy harvester in Autodesk Inventor

The flowchart of the created 3D model in Autodesk inventor is shown in Figure 7. First, a 2D sketch of components of the model is drawn in Autodesk Inventor and converted to a 3D model made of assembled

components as depicted in Figure 8. It consists of a steel frame and a set of blocks for attachment of the three linear springs, a torsional spring and the airfoil shaped wing as a base structure for the piezoelectric cantilever beam.



**Figure 8: 3D Autodesk Inventor model of the piezoelectric energy harvester.**

In order to fully illustrate the methodology used in the analytical section, ANSYS simulation software is used to carry out finite element analysis (FEA) and the flowchart is shown in Figure 9.

First, the 3D model is imported as geometry into the ANSYS Fluent to study the effect of air flow over the airfoil and the amount dynamic and static surface pressure generated along with the associated lift and pitching

moment on the wing. The static pressures are imported as surface pressure forces and moments into the ANSYS transient solver where the stress and deformation of the piezoelectric beam is studied. Finally, an electromechanical coupling is carried out with ANSYS piezoelectric ACT (Application Customization Toolkit) extension solver to determine the amount of voltage, current and power generated by the energy harvester.

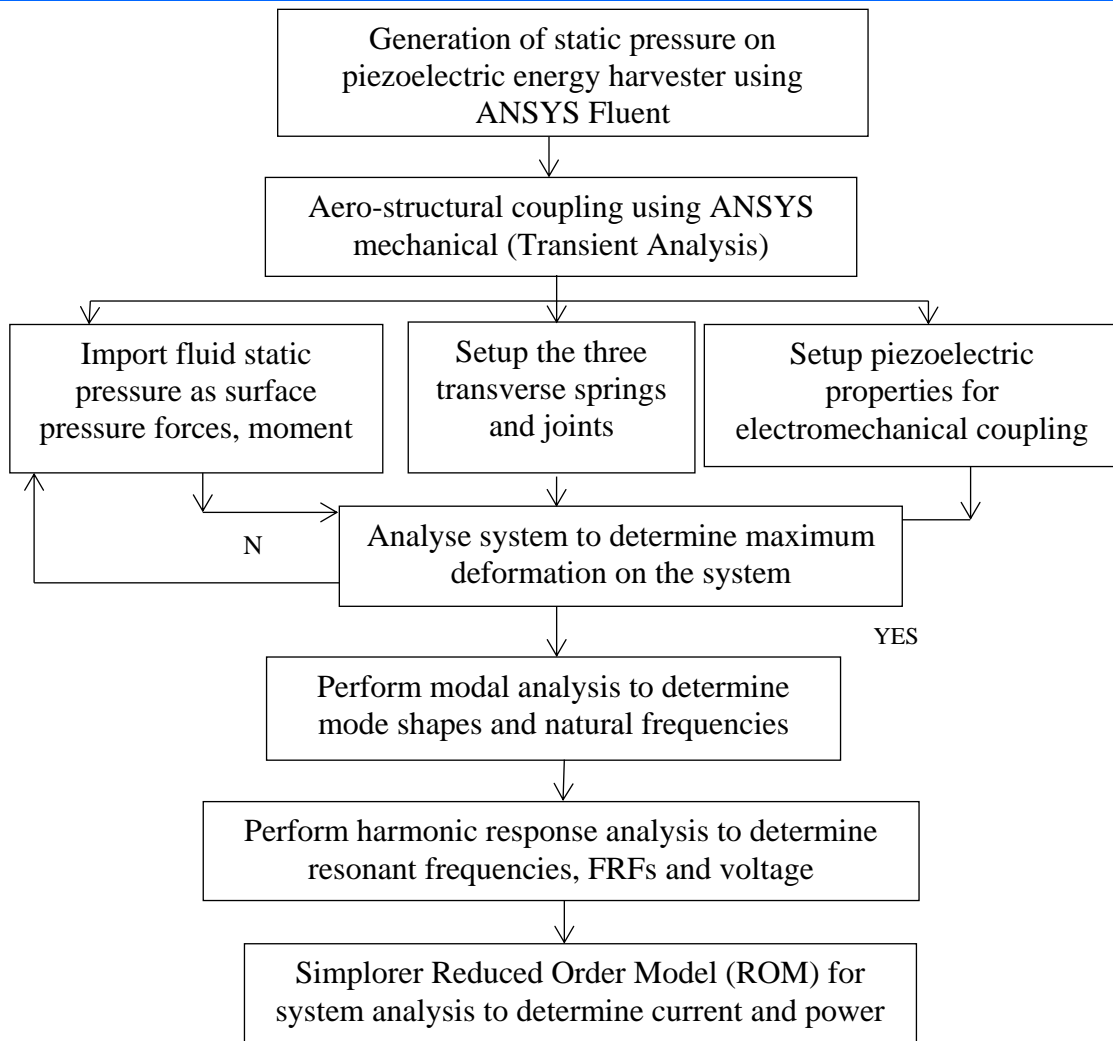


**Figure 9: ANSYS workflow for modelling the piezoelectric energy harvester.**

Next, airfoil static pressure generation with ANSYS fluent was carried out. ANSYS Fluent is a state-of-the-art computer program for modelling fluid flow, heat transfer, and chemical reactions in complex geometries. ANSYS Fluent is written in the C computer language. ANSYS

Fluent provides complete mesh flexibility, including the ability to solve fluid-flow problems (Noe *et al.*, 2014)

The 3D model designed in Autodesk Inventor was imported into ANSYS Fluent where an enclosure representing the air fluid environment (wind tunnel) was created as shown in Figure 3.10.

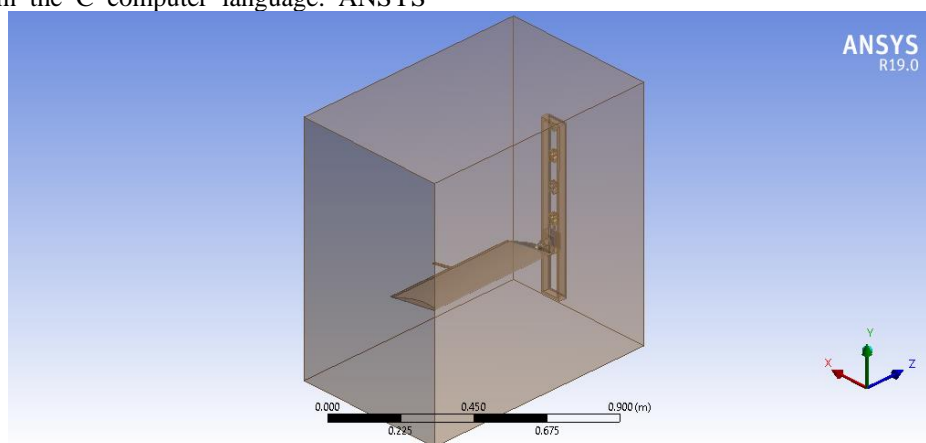


**Figure 3.10: An enclosure representing air fluid flow environment.**

The model of ANSYS was developed base on the proposed analytical model. The electromechanical analysis was carried out with Computational fluid dynamics

package of the ANSYS simulation software to the wind induced vibrations, required for harvesting energy through a dedicated electromechanical coupling technique for the plunge and pitch motion modelled in the analytical section.

The wind induces a vibration on the beam which produces a continuous plunging and pitching motion that excites the piezoelectric beam to undergo electromechanical stress and strain. It is this dynamic deformation that is being coupled to the modal analysis tools to obtain the mode shapes, fundamental resonance frequencies. The objective is to determine the voltage, current and power generated by the system, a harmonic analysis was carried out to generate the voltage frequency response of the piezoelectric beam. The results were exported from ANSYS in an excel spread sheet to MATLAB in order to do a close comparison with the analytical models. Some. The output graphs of the current, power and voltages from ANSYS were imported into MATLAB

In the analytical model, it was established from the results that the highest voltage, current and power generation occurs at the open-circuit condition with a load resistance of  $R_l = 33 T\Omega$ ,  $R_l = 0.3 T\Omega$  and  $R_l = 3 T\Omega$

respectively. The ANSYS simulation was conducted at this load resistance to validate the analytical model developed in this work.

### Validation of Frequency Response of the Voltage Output

The result of the comparison between the analytical and ANSYS simulation results of voltage output for plunge is presented in Figure 11. It can be observed that the resonance frequencies for both cases are a bit different, for example, plunge first resonance occurred at 76.5 Hz for the the analytical frequency ( $f_{ar}$ ) and ANSYS simulation occurred at 100 Hz ( $f_{sr}$ ). Also, the maximum plunge voltage for both cases are 8650/15220 mV and occurred at the third resonance frequency of 676.5/520 Hz respectively.

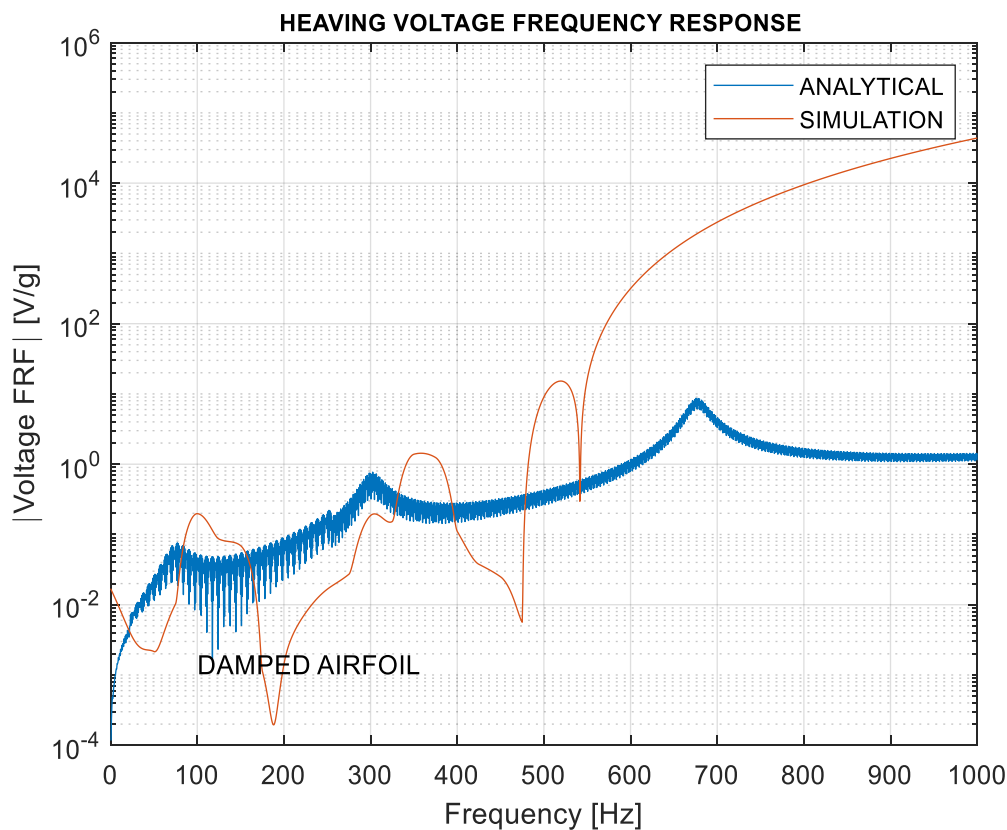


**Figure 11: Analytical and experimental comparison of voltage FRF output under airfoil base plunge excitation at load resistance of  $33 T\Omega$**

The discrepancy as shown in Figure 11 between the simulation and analytical frequency values fluctuates in the range of 10 – 23% in all of the three considered fundamental frequencies. The percentage error on the

values of the maximum output voltages for the third mode is in an average not larger than 44%.

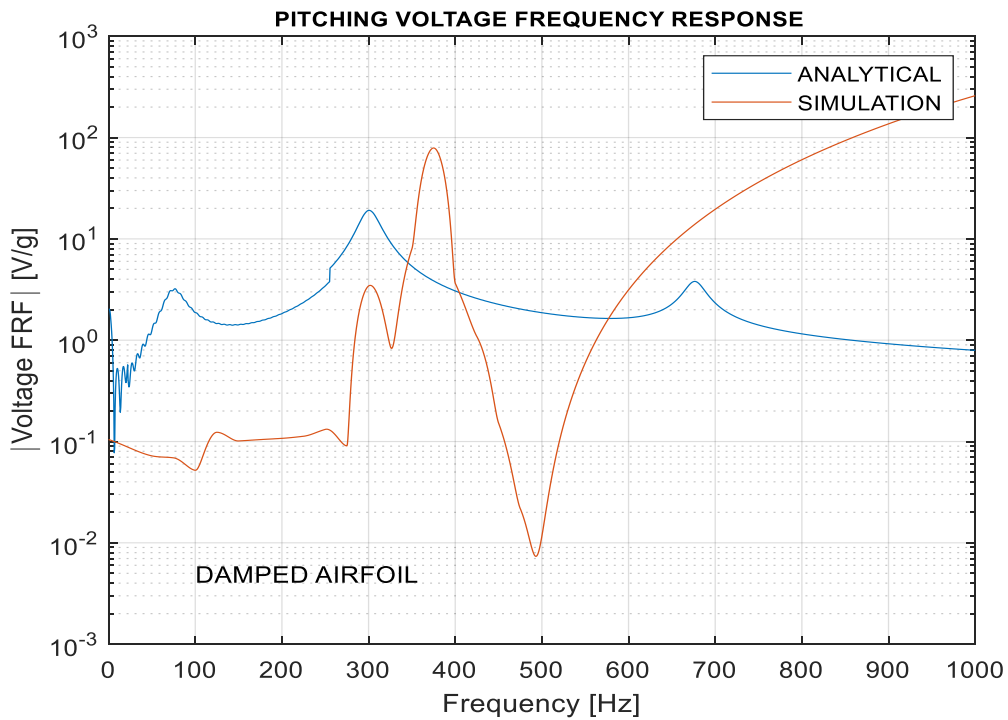


**Figure 12: Analytical and experimental comparison of voltage FRF output under airfoil base pitching excitation at load resistance of  $33 T\Omega$**

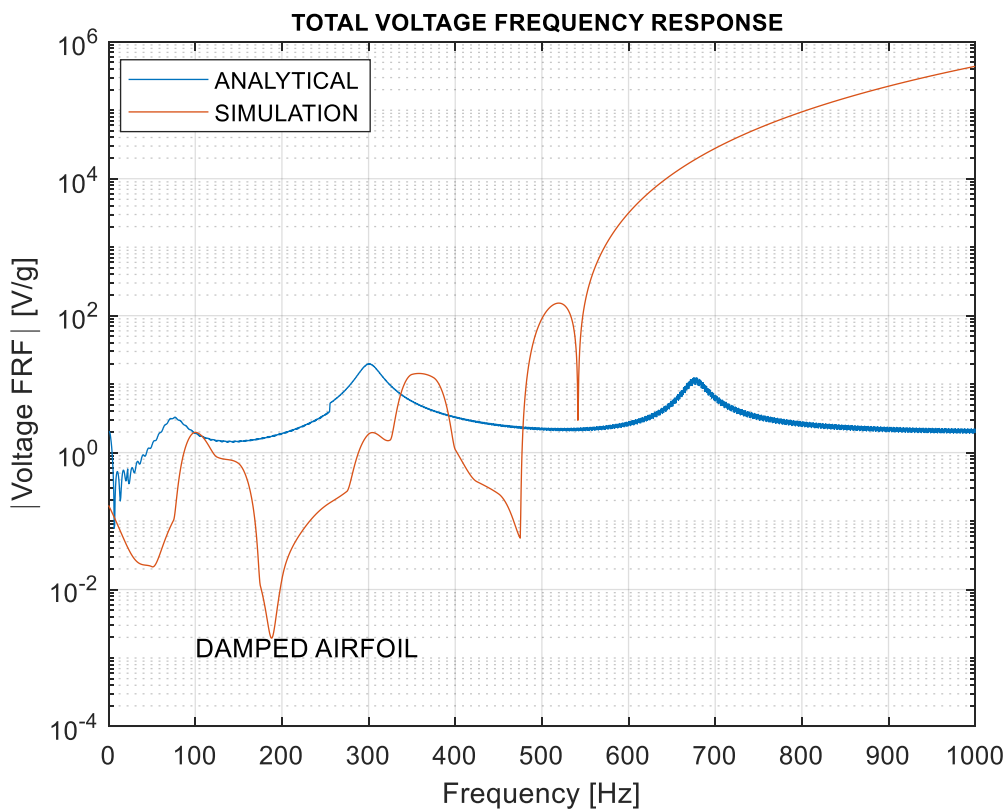


**Figure 13: Analytical and experimental comparison of total voltage FRF output under airfoil base plunge and pitching excitation combined at load resistance of  $33 T\Omega$**

The voltage generated under pitching aerodynamic motion of the system as shown in Figure 12. It can be observed that the resonance frequencies for both

cases are a bit different, the pitch first resonance occurred at 76.5/124 Hz for the first mode. It was also noticed that maximum pitch voltage for both cases are 3804/7892 mV and occurred at the third resonance frequency of 676.5/375 Hz. There are some discrepancy between the simulation and analytical frequency values and these fluctuates in the range of 10 – 40% in all of the three considered fundamental frequencies during aerodynamic pitching.

The system voltage comparison is given in Figure 13. The plunge and pitch voltages are superimposed on one another to obtain the system overall voltage. It can be observed that the resonance frequencies for both the MATLAB and ANSYS results are different, the system first resonance occurred at 76.5/100 Hz. It is seen in Figure 13 that maximum system voltage for both cases are 12400/15240 mW and occurred at the third resonance frequency of 676.50/519 Hz as in the case of plunge motion.

There is substantial increment in the amount of voltage produce in pitch than in plunge, this is due to the

fact that pitch motion actually subjects the piezoelectric beam into more bending and flexural stress than in plunge, yielding more strain and hence more voltage, and this was clearly validated by both ANSYS and analytical models.

### Validation of Frequency Response of the Current Output

In ANSYS simulation, that the current was obtained by generating reduced order model or ROM, imported into ANSYS Twin Tower builder and coupled the resistive load of  $0.3 T\Omega$ . It can be seen from the plots that there is progressive increment in the current generated as one advance on the frequency range. In Figure 14, the heaving current value increase as the fundamental frequency increased, both in analytical and ANSYS simulation models analysis as shown. The first resonance occurs at 776.5100 Hz and its corresponding maximum current occurred at the third resonance frequency of 676.50/519.5 Hz with a value of 9.61/45.73 mA for both analytical and ANSYS simulation respectively.

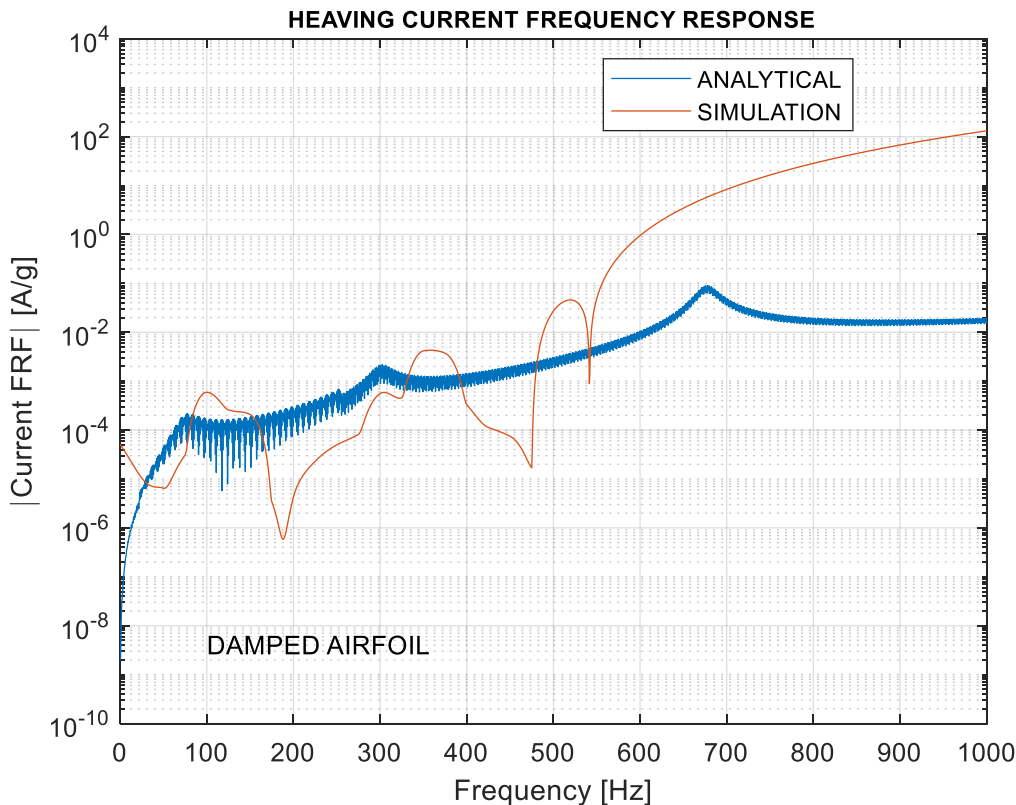


**Figure 14: Analytical and experimental comparison of Current FRF output under airfoil base heaving excitation at load resistance of  $0.3 T\Omega$**

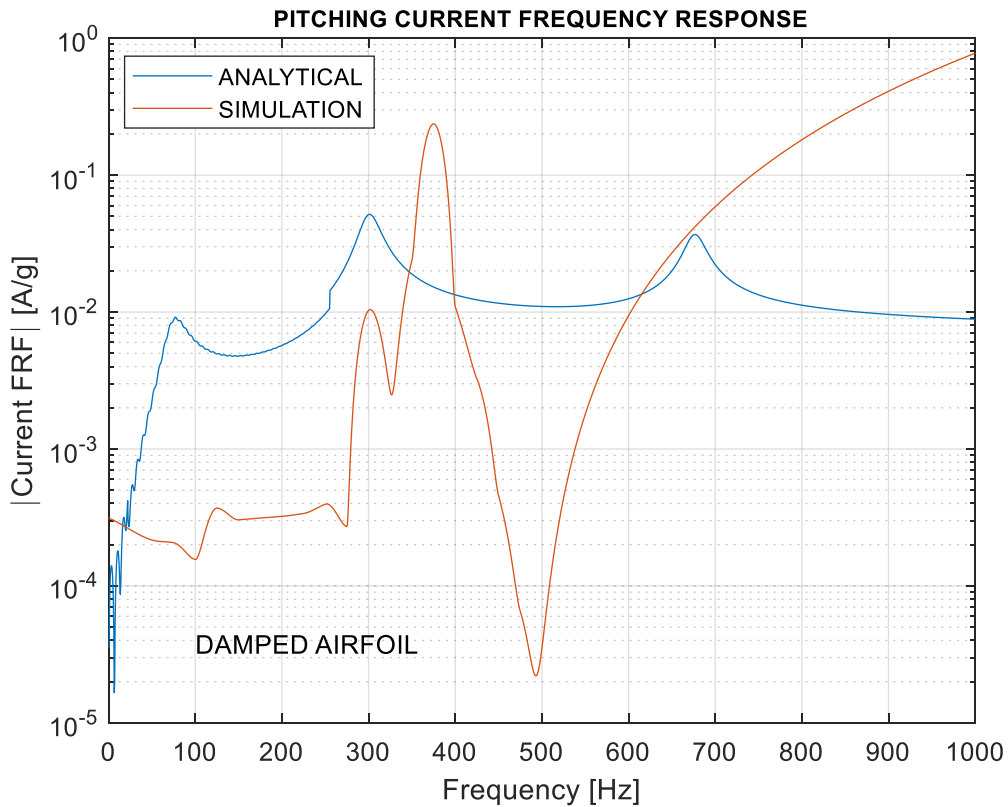


**Figure 15: Analytical and experimental comparison of Current FRF output under airfoil base pitching excitation at load resistance of  $0.3 T\Omega$**

As illustrated in Figure 15, the first resonance occurs at 76.5/100 Hz and its corresponding maximum current occurred at the third resonance frequency of 676.50/519.5 Hz with a corresponding pitching current output value of 40.17/236.6 mA. There is a percentage

error of the frequency values between the simulation and analytical frequency in the range of 0.001 – 40% in all of the three considered fundamental frequencies during aerodynamic pitching.

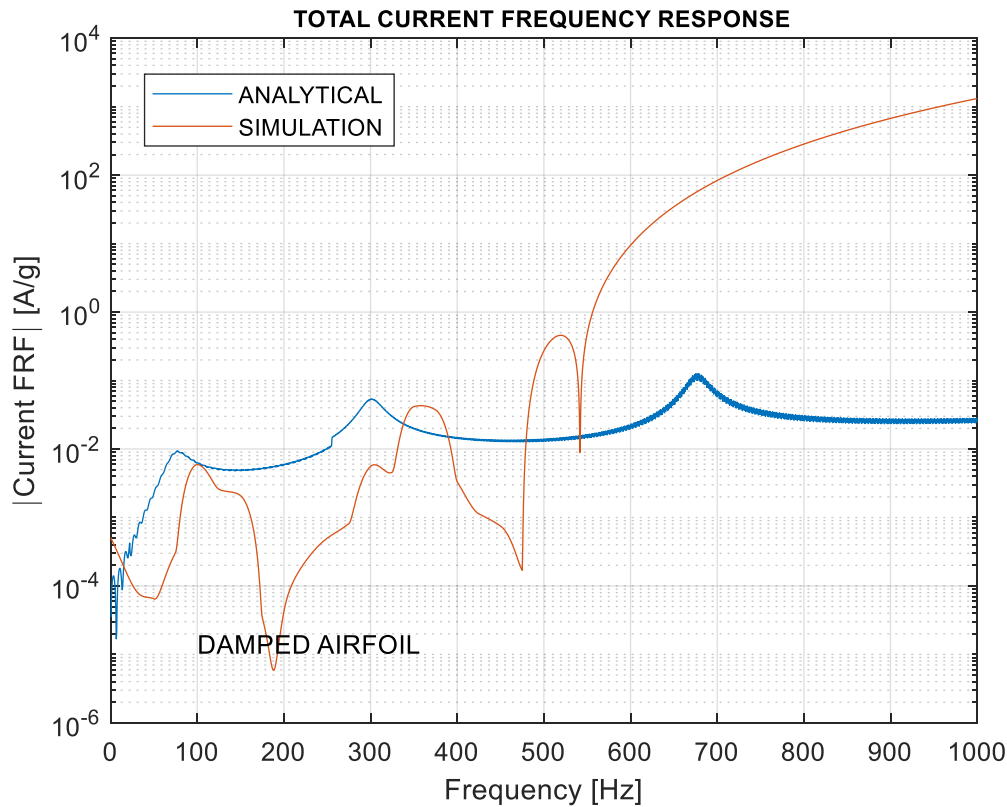


**Figure 16: Analytical and experimental comparison of Total Current FRF output under airfoil base plunge and pitching excitation combined at load resistance of  $0.3 T\Omega$**

The Total current comparisons are given in Figure 16. The plunge and pitch voltages are superimposed on one another to obtain the system overall current. It can be observed that the maximum system current for both analytical and simulation are 136.10/457.30 mA and their corresponding resonance frequencies are 676.5/519.5 Hz occurred at the third resonance frequency. In the overall system, there is a slight reduction in the level of errors or discrepancies in the values of fundamental frequencies and the current output, when compared to the pitching current output.

#### Validation of Frequency Response of the Power Output

The power generated in the analytical was calculated using ohm's law formula ( $V^2/R$ ). This power value was

obtained when simulating with ANSYS Twin Builder or Simplerer. The power output comparison is very essential as this is the parameter with which piezoelectric energy harvester is rated. Figure 17 shows the power output plots at the first three modes. In the heaving motion, the first resonance frequency occurred at 76.5/100 Hz while the maximum power was registered at the third resonance frequency of 676.5/519.5 Hz with a value of 12900/69.72 mW for both analytical and simulation models respectively. The maximum recorded disparity or error in frequency between analytical power model and the ANSYS models was found to be 23%. The power generated from simulation is significantly lower due to the fact that the piezoelectric beam undergoes less deformation in this degree of freedom.

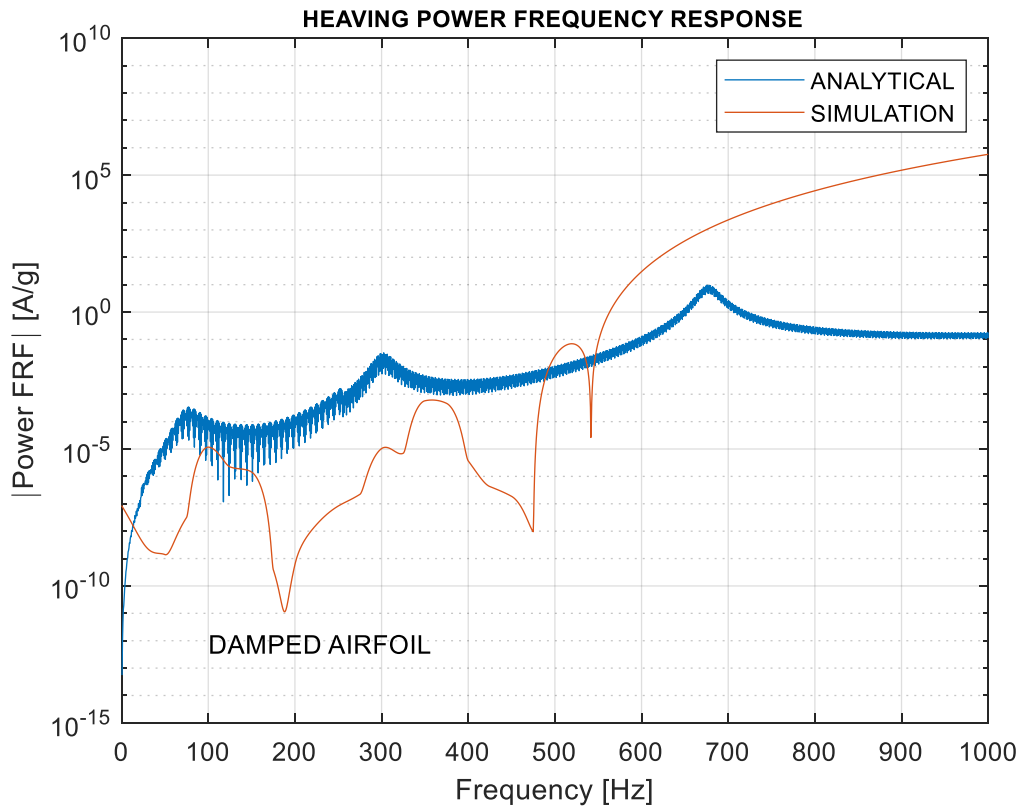


Figure 17: Analytical and experimental comparison of Power FRF output under airfoil base plunge excitation at load resistance of  $3 T\Omega$

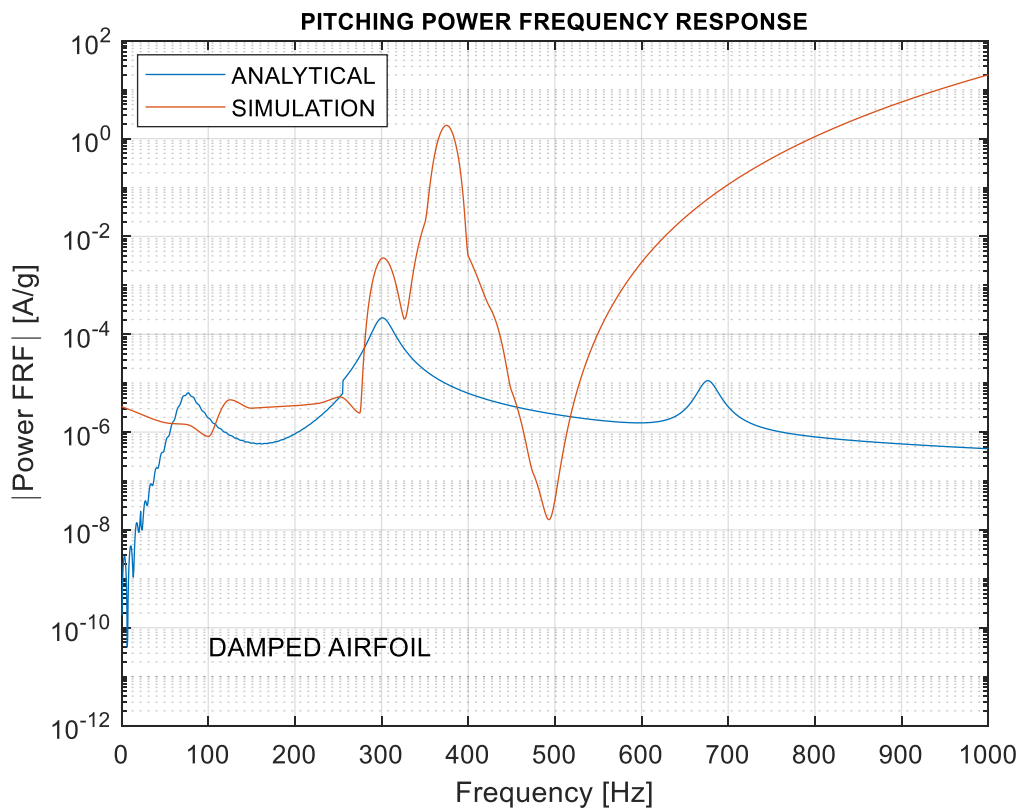
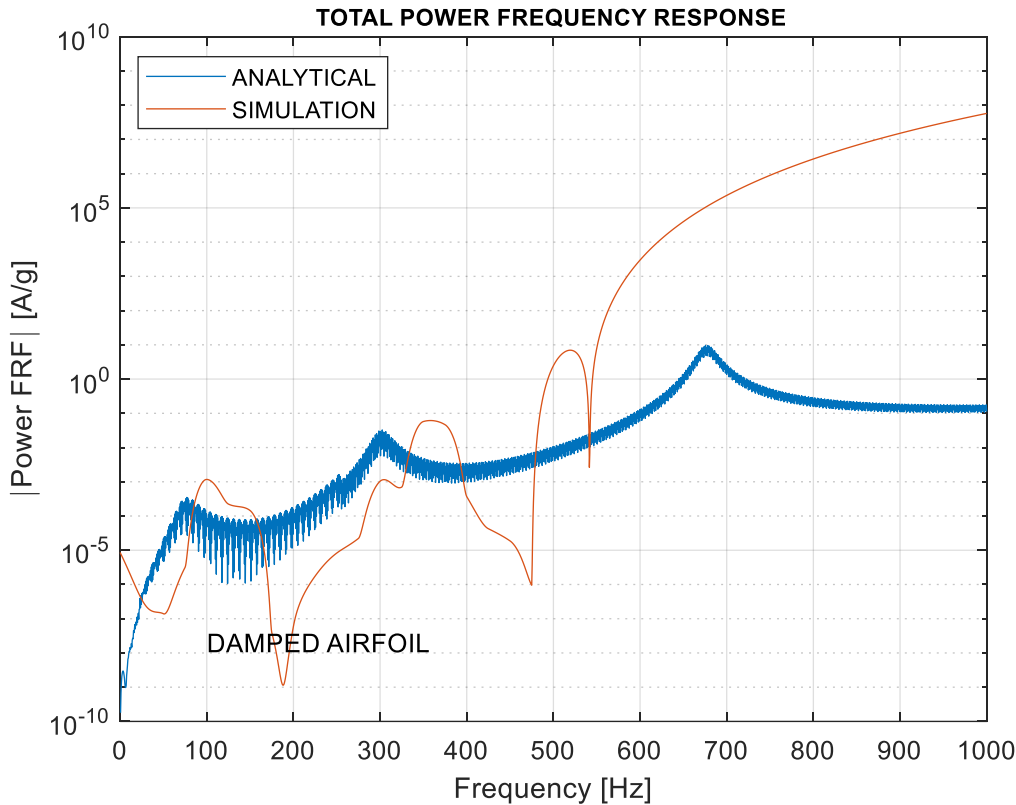


Figure 18: Analytical and experimental comparison of Power FRF output under airfoil base pitching excitation at load resistance of  $3 T\Omega$

The pitch motion generates power which progressively increased along the frequency range of as illustrated in Figure 18. The first resonance occurred at a frequency of 76.5/124 Hz and the maximum power seems to stay at the third resonance frequency of 676.5/519.5 Hz with a value of 0.014/18680 mW for both analytical and simulation models respectively. The maximum

recorded disparity or percentage error in frequency between analytical pitch power model and the pitch simulation was found to be 45%. The power produced in pitch degree of freedom is higher than in heaving, due to a higher deformation in this degree of freedom.



**Figure 19: Analytical and experimental comparison of Total Power FRF output under airfoil base heaving and pitching excitation combined at load resistance of  $3 T\Omega$**

The total system power output is shown in Figure 19. In the total system analysis, the first resonance frequency occurred at a frequency of 76.5/100 Hz and the maximum system power still stays at resonance frequency of 676.5/519.5 Hz with a value of 12900/69720 mW. There has been a higher contribution to voltage, current and power generation from the pitch degree of freedom than the plunge because this axis offered more deformation in the piezoelectric beam, an indication of a higher aero-structural and electromagnetic coupling within the system.

It is observed that the analytical and ANSYS software solutions registered an average percentage error in resonance frequency of less than 8% while the average percentage error for voltage, current and power generated was less than 41%. It is illustrated both by analytical and simulation models that the maximum system voltage, current and power can be obtained if the system is

designed to resonate more on its third resonance frequency.

## VI. COMPARISON OF PRESENT WORK WITH PREVIOUS RESEARCH WORKS

In the development of micro electromechanical systems, most especially in miniature piezoelectric power generators, many researches have been carried out to innovate on better approach to generate higher power from these systems. In that quest, this research work was embarked upon to determine which energy source and method of coupling that would yield higher power values when combined in design. There has been one common procedure adopted by most of these researchers, that is, to harvest the energy in only one degree of freedom and consider only one type of coupling. This paper made a considerable attempt to consider two degree of freedom.

**Table 1: Comparison between present work and selected other research papers**

References	Material Type	Peak Power (mW)	Volume	Frequency (Hz)	Excitation Force
<b>This Work, 2020</b>	<b>PZT ceramics</b>	<b>12900</b>	<b>1.95 cm<sup>3</sup></b>	<b>676.5</b>	<b>10.5 N</b>
Mohammadi, 2003	PZT fiber	120	2.2cm <sup>3</sup>	-	-
Kim, 2004	PZT ceramics	39	1cm <sup>3</sup>	100	7.8 N
Kim, 2005	PZT ceramics	52	1.5cm <sup>3</sup>	100	70 N
Liya et al., 2017	PZT ceramics	4.48		-	-
Aktakka 2012	PZT ceramics	0.205	27 mm <sup>3</sup>	154	-
Gu et al., 2013	PZT nano fibers	4.9	-	-	
Park et al., 2014	PZT thin film	3	-	-	-
Sodano et al., 2003	PZT ceramic	30	-	-	
Tang et al., 2012	PZT ceramic	28.8			

Source: Mohammadi, 2003; Kim et al., 2004; Kim et al, 2005; Liya et al., 2017; Aktakka 2012; Gu et al., 2013; Park et al., 2014; Sodano et al., 2003; Tang et al., 2012

## VII. CONCLUSION

The newly introduced coupling ensured the aligning of the aerodynamic forces and moments from the ambient air as they interact with the structural and the electrical domain. Despite having a small volume this harvester generates more power than its counterparts as shown in Table 4.24. The airflow oscillation induced excitation force of 10.5 N was generated to excite the base structure and a power of 12900 mW was produced at third resonance frequency of 676.5 Hz. Although lower power is generated at other resonance frequencies, the third fundamental frequency seems to pitch it all. The summary of the comparison as tabulated in Table 4.24 shows that the improvement over previous efforts has been proven to be remarkably high. The efficacy of the analytical model can further be validated with physical experimentation of the proposed design.

### Reference

Akorode, M. F., Ibrahim, O., Amuda, S. A., Otuze, A. O. and Olufeagba, B. J. (2017). Current status and outlook of renewable energy development in Nigeria. *Nigeria Journal of Technology (NIJOTECH)*, 36(1):196 - 212.

Aktakka, E. E. (2012). *Integration of Bulk Piezoelectric Materials Into Mirosystems*. PhD Thesis, University of Michigan, USA

Alighanbari, H. (1995). *Flutter Analysis and Chaotic Response of an Airfoil Accounting for Structural Nonlinearities*. PhD Thesis, McGill University, Canada.

Anderson, J. D. (2001). *Fundamentals of Aerodynamics*. 3<sup>rd</sup> Edition. McGraw Hill, Newyork

Daochun L., Xiang, J., and Ronch, A. D. (2016). A modified airfoil-based piezoaeroelastic energy harvester with double plunge degree of freedom. *Theoretical and Applied Mechanics Letters*, 16 (2): 244-247.

Dias, J. A. C., Marqui, C. De. Jr., and Erturk A. (2013). Hybrid piezoelectric-inductive flow energy harvesting and dimensionless electroaeroelastic analysis for scaling. *Applied Physics Letters*, (102): 1-5.

Elfrink, R., Kamel, T. M., Goedbloed, M., Matova, S., Hohlfield, D., Andel, Y. V. and Schaijk, R. V. (2016). Vibration energy harvesting with aluminum nitride-based piezoelectric devices. *Journal of Micromechanics and Micro-Engineering*, 19(9): 9-25.

Gu, L., Cui, N.Y., Cheng, L., Xu, Q, Bai, S., Yuan, M. M., Wu, W. W., Liu, J. M., Zhao, Y. and Fei, M. (2013). Flexible fiber nanogenerator with 209 V output voltage directly powers a light-emitting diode. *Nano Lett*, 13(1): 91–94.

Guruswamy, P. and Yang, T. Y. (1981). Aeroelastic time response analysis of thin airfoils by transonic code LTRAN2. *Computers and Fluids*, 9(4): 409-425.

Hu, Z., Qiu, J., Wang, X., Gao, Y., Liu, X., Chang, Q., Long, Y., and He, X. (2018). An integrated multi-source energy harvester based on vibration and magnetic field energy. *AIP Advances*, 8: 1-9

Khan, F. U. and Iqbal, M. (2018). Electromagnetic bridge energy harvester utilizing bridge's vibrations and ambient wind for wireless sensor node application. *Journal Sensors*, (3):1-18.

Kim, H. W., Priyal, S., Kenji U., Uchino, K. and Newham, R. E. (2005). Piezoelectric energy harvesting under high pre-stressed cyclic vibrations, *Journal of Electroceramics*, (15): 27-34

Kim, H. W., Amit, B., Priyal, S., Kenji U., Douglas, M., Newham, R. E. and Hofman, H. F. (2004). Energy harvesting using a piezoelectric "cymbal" transducer in dynamic environment, *Japanese Journal of Applied Physics*, (9):1 - 14

Iranmanesh, E., Rasheed, A., Li, W. and Wang, K. (2018). A wearable piezoelectric energy harvester rectified by a dual-gate thin-film transistor. *IEEE Transactions on Electron Devices*, 65(2): 542-546.

Leon-Gil, J.A., Cortes-Loredo, A., Fabian-Mijangos, A., Martinez-Flores, J. J., Tovar-Padilla, M., Cardona-Castro, M. A., Morales-Sanchez, A., and Alvarez-Quintana, J. (2018) Medium and short wave RF energy harvester for power wireless sensor network. *Sensors*, 19: 1-13

- Liya, Z., Lihua, T., Junrui, L. and Yaowen, Y. (2017). Synergy of wind energy harvesting and synchronized switch harvesting interface circuit. *IEEE/ASME Transactions of Mechatronics*, 22(2): 1093-1103
- Mackenzie, J. D. and Ho, C. (2015). Perspective on energy storage for flexible electronics systems. *Proc. IEEE*, (103): 535-553.
- Mohammadi, F., Khan, A. and Cass, R. B. (2003) Electronics on Unconventional Substrates- Electrotextiles and Giant-Area Flexible Circuits, *Mater. Res. Soc. Symp. Proc*, (736): 263 – 268.
- Nandi, D.B., Odeh, C. I. and Omeje, C.O. (2017). A maximum power point tracking scheme for a 1 KW stand-alone solar energy based power supply. *Nigerian Journal of Technology (NIJOTECH)*. 36(2): 582-593.
- Noe, F. M., Noor H. A. R., Sherif A. A. and Sharifah A. S. (2014). Computational fluid dynamics (CFD) modeling of pulverized coal combustion processes in a 700 MW wall tangentially- fired boiler. *Journal of Applied Science and Agriculture*, 9(11): 190 – 194
- Ono, S., Miwa, K., Iori, J., Mitsuya, H., Ishibashi, K., Sano, C., Toshiyoshi, H. and Fujita, H. (2016). A novel vibrational energy harvester with electric double layer electrets. *Journal of Physics: Conference Series*. 7(4): 1-4.
- Park, K. I., Son, J. H., Hwang, G. T., Jeong, C. K., Ryu, J., Koo, M., Choi, I., Lee, S. H., Byun, M., and Wang, Z. L. (2014). Highly-efficient, flexible piezoelectric PZT thin film nanogenerator on plastic substrates. *Adv. Mater.* 1(26): 2514–2520.
- Podder, P., Constantinou, P., Amann, A. and Roy, S. (2016). Frequency adjustable MEMS vibration energy harvester. *Journal Physics: Conference Series*. (757): 1-6.
- Rashid, A., Khan, F., Gul, T., Fakhr-e-Alam, Ali S., Khan, S. and Khalil, F. K. (2018). Improving energy conservation in wireless sensor networks using energy harvesting system. *International Journal of Advanced Computer Science and Applications*, 9(1): 1-8.
- Rizman, Z. I., Yassin I.M., Zaman, F. K., Hashim, F. R., and Yeap, K. H. (2018). Smart multi-application energy harvesting using arduino. *Journal of Fundamental and Applied Science*, (10): 689-704.
- Sherazi, H. H., and Grieco, L. A. and Boggia, G. (2018). A comprehensive review on energy harvesting MAC protocols in WSNs: challenges and tradeoffs. *Ad Hoc Network*. (71): 117-134.
- Sodano, H A., Gyuhae P., Donald, J. L. and Daniel J. I. (2003). Use of piezoelectric energy harvesting devices for charging batteries, *Proc. SPIE 5050*, 101–108
- Tang, G., Liu, J. Q., Yang, B., Luo, J. B., Liu, H. S., Li, Y. G., Yang, C. S., He, D. N., Dao, V. D., Tanaka, K. (2012). Fabrication and analysis of high-performance piezoelectric MEMS generators. *J. Micromech. Microeng*, 2: 1-11.
- Zeng, Z., Ren, B., Gai, L., Zhao, X., Luo, H. and Wang, D. (2016). Shear-mode-based cantilever driving low-frequency piezoelectric energy harvester using 0.67Pb (Mg<sub>1/3</sub>Nb<sub>2/3</sub>)O<sub>3</sub>-0.33PbTiO<sub>3</sub>. *IEEE Transactions on Ultrasonics, Ferroelectrics, and Frequency Control*, 63(8): 1192-1197.